Sonochemical Synthesis of Mesoporous Iron Oxide and Accounts of Its Magnetic and Catalytic Properties

D. N. Srivastava,[†] N. Perkas,[†] A. Gedanken,*[,†] and I. Felner[‡]

Department of Chemistry, Bar-Ilan University, Ramat-Gan 52900, Israel, and The Racah Institute of Physics, The Hebrew University, Jerusalem 91904, Israel

Received: August 31, 2001

Synthesis of mesoporous iron oxides has been reported using a sonochemical technique. Iron(III) ethoxide was used as an inorganic precursor and CTAB as an organic structure directing agent. After sonication the surfactant was removed by calcination and solvent extraction methods. FTIR spectra demonstrated the removal of the surfactant from the pores of the mesoporous iron oxide. The calcinated material was characterized by XRD, TEM, TGA, and BET surface area measurements. The surface area after solvent extraction is found to be 274 m^2/g. The magnetic and catalytic properties of the materials have been studied. The as-prepared amorphous Fe_2O_3 has shown a paramagnetic behavior, while after calcination at 350 °C it changes to γ-Fe_2O_3 with good magnetic properties. The catalytic activity of mesoporous iron oxide was studied in the reaction of cyclohexane oxidation under mild conditions. The mesoporous Fe_2O_3 catalyst has shown high conversion of cyclohexane into cyclohexanone and cyclohexanol, with a high selectivity.

I. Introduction

Contemporary efforts in chemistry and physics proved iron oxides in its various phases as an interesting and important class of materials. The current and prospective fields include chemical industry, biotechnology, medicine, electromagnetic devices,[1−5] and magnetoelectronics.[6] The properties of these materials are extensively dependent on the shape, size, and structures, leading to a growing interest in the nanoscale science, meaning thereby science, engineering, and technology concerned with the manipulation of the matter on the nanometer length scale. The main idea is to study the properties, interactions, and processing of units containing a countable number of atoms.[7]

Mesoporous materials are another important class of materials. Following its discovery around 8 years ago,[8] these materials now occupy a superb position in materials science.[9] According to IUPAC classification, the inorganic solids that contain pores with diameters in the 10−100 Å size range are considered as mesoporous. These pores greatly increase the surface area/volume ratio of a material, making them very useful in the surface related applications, for example biosensors,[10−11] other sensors such as humidity[12] and volatile organic solvent[13] sensors, electric double layer,[14−15] electrorheological properties,[16] electrical junction properties,[17] solar cells,[18−20] mimicking photosynthesis,[21] and optical applications.[22−23]

Apart from all these application, magnetic properties of the iron oxides and their nanoparticles are also very important. A lot of interest has been focused on the studies of magnetic properties of Fe-based material impregnated in the pores of mesoporous materials. Manners et al. reported on the synthesis of poly(ferrocenylsilanes) inside the pores of mesoporous silica.[24] When pyrolyzed at 900 °C in a nitrogen atmosphere, the mesoporous silica/ferrocenylailane composite yielded Fe nanoparticles in the 30−40 Å channel of MCM-41. Characterization of the magnetic properties of the product in the channel of mesoporous silica indicated that the clusters were superparamagnetic. A new family of mesoporous niobium oxide−bis(cyclopentadienyl) nickel composites that exhibit either superparamagnetic or spin glass behavior, depending on the loading level of the bis(cyclopentadienyl) nickel in the pore, has been reported.[25] In a slightly different way, Stucky et al. have reported the synthesis and magnetic properties of the ordered, lamellar, iron oxide/surfactant composites.[26] A redox chemical procedure and the variable solubility of iron in solution have been used to form the composite, which yielded a controlled thickness of inorganic layers. These materials displayed super-antiferromagnetism. Other similar attempts at depositing magnetic materials in the mesoporous materials can be found.[27−28]

Another very important application of the nanoparticles in general, and mesoporous materials in particular, is in catalysis. Several iron-based materials have been used in various catalytic applications. For example, it has been used in the production of clean transportation fuels and high molecular weight hydrocarbons from synthesis gas (H_2/CO mixture) by Fischer-Tropsch synthesis.[29] An amorphous α-Fe_2O_3 thin film deposited on a fused quartz substrate has shown photocatalytic degradation of an oxygenated aqueous solution of phenol upon visible light illumination.[30] Several authors have extensively reviewed the application of the mesoporous materials in catalysis.[31−32] Similar to magnetic properties, catalytic properties have also been studied after filling the catalysts inside the pores of the mesoporous framework. Previous such studies have shown considerably high conversion of cyclohexane to cyclohexanol and cyclohexanone.[33]

From the above discussion, it is clear that, in most cases, the materials having magnetic and catalytic properties are been filled in mesoporous materials. Here we present our results of the synthesis and properties of mesoporous iron oxide. We prepared mesoporous Fe_2O_3 by a sonochemical method and studied its magnetic and catalytic properties.

* Author to whom correspondence should be addressed. E-mail: gedanken@mail.biu.ac.il.
[†] Bar-Ilan University.
[‡] The Hebrew University.

10.1021/jp015532w CCC: $22.00
Published on Web 01/17/2002

II. Experimental Section

The mesoporous Fe_2O_3 was prepared by a supra molecular templating method, using a sonochemical technique and iron(III) ethoxide (Alfa Aesar) and cetyltrimethylammonium bromide (CTAB) (Sigma) as an inorganic precursor and surfactant, respectively. The following procedure has been adopted: 2.5 mmol. of iron ethoxide was put in a sonication flask and a solution of 1 mmol of CTAB in 20 mL of ethanol was added to that followed by 60 mL of double distilled water. The solution was then made basic by adding 40 mL of NH_4OH and pH was adjusted to 10.6. The NH_4OH and ethanol used were of AR grade. The system was then irradiated with a high-intensity ultrasonic horn (Ti-horn, 20 kHz, and 100 W/cm^2 at 65% efficiency) under air for 3 h. After the sonication, the precipitate was centrifuged at 9000 rpm and washed with distilled water until the smell of ammonia was removed. The precipitate was dried under vacuum and termed as "as-prepared sample". The surfactant was removed from the pores of the as-prepared sample either by heating or by extraction with ethanol.

Both the as-prepared and treated samples were characterized by various methods. The XRD measurements were carried out with a Bruker X-ray diffractometer D_8 using Cu Kα radiation. The thermogravimetric analysis was carried out using a Mettler TGA/STDA 851. The transmission electron micrographs were obtained with a JEOL-JEM 100 SX electron microscope. Samples for the TEM experiments were prepared by suspending dried samples in absolute ethanol. A drop of the sample suspension was allowed to dry on a copper grid (400 mesh, Electro Microscopy Sciences) coated with a carbon film. The IR spectra were recorded by a Nicolet Impact 410 infrared spectrophotometer in KBr medium. The surface area of these samples was measured by Micromeritics (Gemini 2375) surface area analyzer. The nitrogen adsorption and desorption isotherms were measured at 77 K temperature after heating the sample at 150 °C for 2 h. The Mössbauer spectroscopy (MS) studies were carried out using a conventional constant acceleration spectrometer. The ^{57}Fe MS were measured with a mCi ^{57}Co:Rh source, and the spectra were least-squares fitted with two sub spectra. The isomer shift (IS) values are relative to Fe metal at 300 K. The magnetic measurements were performed on a vibrating sample magnetometer (VSM-Oxford-3001).

To study the catalytic activity, the cyclohexane was purified first, by distillation over calcium hydride. The oxidation reactions were performed in a thermostated glass reactor using 2 mL (18.5 mmol) of cyclohexane, 2.5 mL (27.75 mmol) of isobutyraldehyde (molar ratio 1.5:1), a catalytic amount of acetic acid—0.06 mL (1 mmol) and 0.15 mmol of catalyst. The reaction mixture was stirred on a magnetic stirer at 1 atm of oxygen and 70 °C for 15−17 h. The reaction products were analyzed by gas chromatography, using Varian-400, equipped with a packed column (10% Carbowax 400 on Chromosorb 101). The starting alkane was used as an internal standard. Conversion was defined as a percentage of the starting alkane converted into products.

III. Results and Discussion

A. Material Characterization. Figure 1 illustrates the IR spectra of the as-prepared, calcinated, and solvent-extracted samples. Two sharp peaks at ~2919 cm^{-1} and ~2846 cm^{-1}, in the as-prepared sample (Figure 1a) are attributed to the stretching vibrations of CH_2 and CH_3 in CTAB, which disappeared after calcination (Figure 1b−d). The intensity of these peaks also decreases after solvent extraction (Figure 1e), and there is no trace of the CTAB peak in the sample extracted at elevated temperature (Figure 1f). This shows the removal of the surfactant from the pores of the iron oxide. A broad band in the IR spectra of the as-prepared sample can be seen at 3403 cm^{-1}, which is attributed to the adsorbed water, which disappeared after calcination. Similarly, the peaks at 1646 and 1467 cm^{-1} are assigned to the water and ammonia, which are also removed after calcination. The peak at 419 cm^{-1} is attributed to the Fe−O bond vibration of the Fe_2O_3; the peak is sharpened after calcination at 350 °C. The wide angle XRD spectra are given in Figure 2 a−d. It can be seen that the as-prepared sample is an amorphous material, although it matches the XRD spectra of hematite (JCPDS-33-0664)(Figure 2a). A similar XRD pattern can be seen for the solvent-extracted sample (Figure 2b). However, after calcination at 350 °C, the structure changes to γ-Fe_2O_3 (maghemite) (JCPDS-39-1346), with sharp X-ray diffraction lines showing increased crystallinity. The same features can be seen for the sample calcinated at 500 °C (Figure 2d). The Mössbauer spectra confirm the presence of 80% γ-Fe_2O_3 in the calcinated sample, which we will be discussing latter in the section describing the magnetic properties. We observed a sharp increase of the signal in the low angle XRD spectra of these samples at around $2\theta = 2°$. However it does not resolve as a peak. The absence of a peak in low angle XRD may be due to the lack of long-range ordering in the crystal or at least restricted to low regions. A possible explanation for the less organized pore structure may be the weaker electrostatic interaction between the surfactant and the inorganic species in our case, as compared with the formation of MCM-41. The models for the formation of mesostructure silica were categorized in a S^+I^- pathway, which involves anionic silicate species

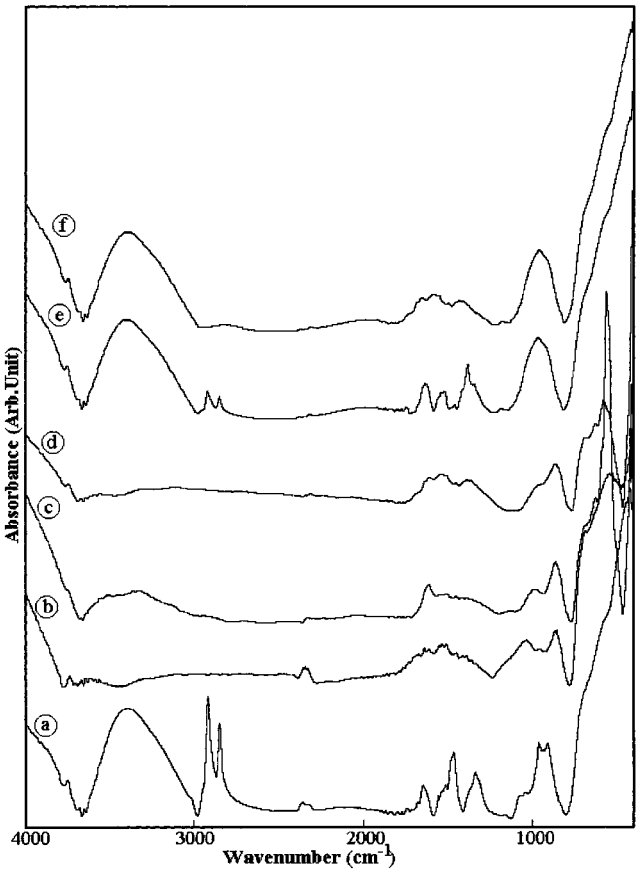

Figure 1. FT/IR spectra of Fe sample: (a) as-prepared, (b) calcinated at 250 °C for 2 h, (c) calcinated at 350 °C for 2 h, (d) calcinated at 250 °C for 4 h, (e) extracted in ethanol for 6 h, (f) extracted in ethanol for 12 h at elevated temperature.

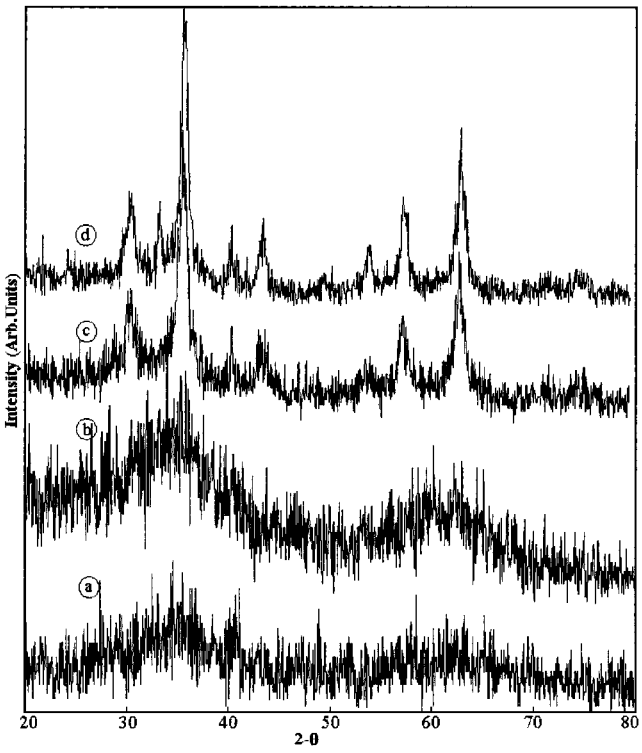

Figure 2. Wide-angle X-ray diffraction patterns of (a) as-prepared material; (b) solvent-extracted sample; (c) after calcination at 350 °C; (d) after calcination at 500 °C.

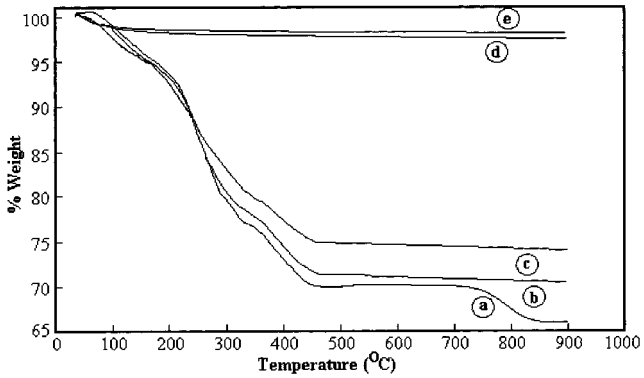

Figure 3. TGA curve of (a) as-prepared material in constant magnetic field; (b) as-prepared material without magnetic field; (c) solvent-extracted sample at room temperature; (d) solvent-extracted sample at elevated temperature; (e) calcinated at 350 °C.

and cationic quaternary ammonium surfactant in high pH. The inorganic component preferentially interacts with the positively charged ammonium headgroups of the surfactant and condensed into a solid continuous framework. The resulting organic−inorganic mesostructure could be alternatively viewed as a hexagonal array of surfactant micellar rods embedded in the silica matrix. Removal of the surfactants produced the open, mesoporous MCM-41 framework. In our case, the bigger size of the iron inorganic species as compared to the silicate may restrict the proper inorganic−organic framework formation leading to less organized mesostructure.

The TGA curve is given in Figure 3 for an iron sample. The as-prepared sample shows that the weight loss occurs in steps, with total loss of 30% up to 400 °C. Above this temperature no weight loss has been observed up to 900 °C (Figure 3b). The initial weight loss of 7−8% is attributed to the loss of adsorbed ammonia and water. The complete removal of surfactant was further confirmed by observing the TGA of the calcinated

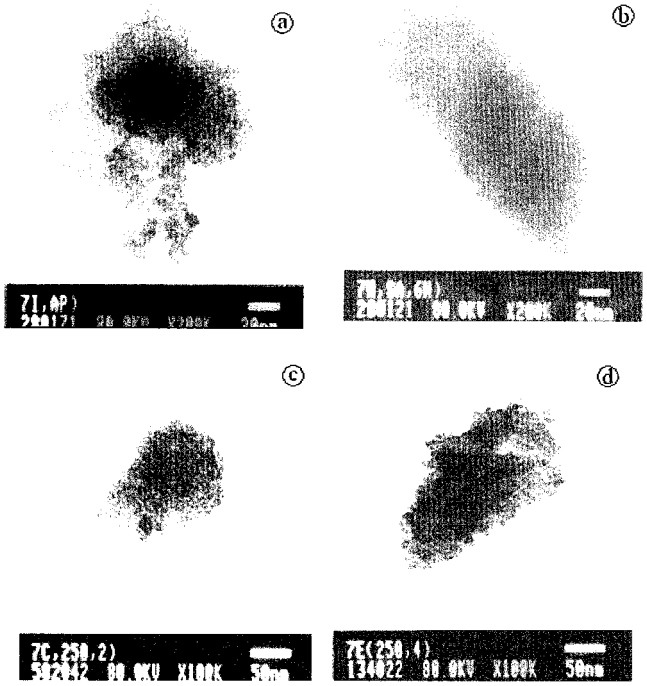

Figure 4. TEM photographs for (a) as-prepared material; (b) after solvent extraction; (c) after calcination at 250 °C for 2 h, (d) after calcination at 250 °C for 4 h.

sample at 500 °C (Figure 3e). We have not seen any weight loss till 900 °C in this sample. A similar TGA has been observed for the samples solvent-extracted at elevated temperature (Figure 3d). However, the extraction at room temperature (rt) has not given a satisfactory result. A weight loss of around 26% has been observed for a room-temperature extracted sample (Figure 3c). The incomplete removal of the surfactant is in accordance with the IR spectra of the sample, and is also reflected in the BET surface area measurements. We also carried out the thermal analysis under a permanent magnetic field (Figure 3a). Up to 500 °C, the general features of the TGA curve in the magnetic field are similar to those without a magnetic field. The weight loss in this spectrum around 825 °C, appearing only for the sample in a magnetic field, is attributed to the loss of magnetic properties of the material, due to thermal agitation (the Neel temperature).

Figure 4 shows the TEM photographs of the as-prepared (4a), after solvent extraction (4b), and after calcination (4c−d) samples. The particles of Fe_2O_3 are of an irregular shape having a 100−200 nm diameter with a small pore size of 3−5 nm average diameter. The pores can be seen in the as-prepared sample. The BET pore size distribution confirms this observation which we will describe later. Uniformity in the pore structure is not visible in the mesostructure and the structure is more likely of a wormhole-like morphology. The solvent-extracted sample also shows a similar structure, but the structure can be seen more clearly here than in as-prepared sample, due to the removal of surfactants from the pores. On the other hand, in the calcinated sample the destruction of the mesostructure is clearly visible. This picture also shows more crystallinity, which is in accordance with the XRD results. The surface area is also found to be reduced in the calcinated sample. The BET surface area measurement shows a total area of 0.8 m^2/g for the as-prepared sample, which increased up to 274 m^2/g after extraction with ethanol for 12 h at elevated temperature. This observation confirms the removal of the surfactant from the pores. The surface area data after different treatments are given in Table 1. It is clear from the table that the surface area does not change

TABLE 1: The BET Surface Area Found in the As-Prepared Sample and after Various Treatments

treatment[a,b]	time of calcination or extraction (hours)	surface area (m^2/g)
as-preparedl		0.80
calcinated at 250 °C	2	151
calcinated at 300 °C	2	140
calcinated at 350 °C	2	110
calcinated at 500 °C	2	94
calcinated at 250 °C	4	177
calcinated at 350 °C	4	110
extracted at r.t.	6	227
extracted at r.t.	12	235
extracted at r.t.	24	239
extracted at e.t.	6	215
extracted at e.t.	12	274
extracted at e.t.	24	274

[a] r.t. is room temperature. [b] e.t. is elevated temperature.

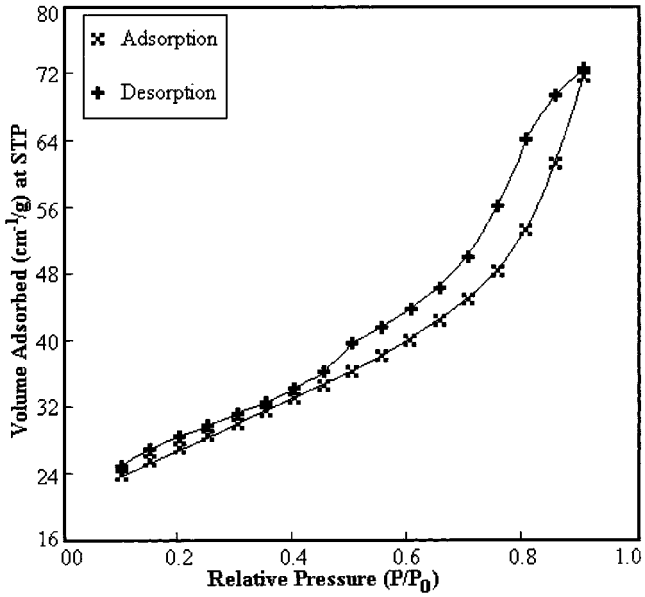

Figure 5. Adsorption−desorption isotherm for Fe_2O_3 mesostructure after extraction with ethanol for 12 h at elevated temperature.

much, after extraction of 24 h, both in the case of room temperature extraction and at elevated temperature extraction, indicating that the extraction of 12 h is sufficient for the removal of the surfactants. Further, the surface area found after extraction at room temperature is a bit less, where a total of 227 m^2/g area has been found. This shows that the extraction at room temperature does not remove all the surfactants and heating is needed for an effective removal of the surfactant. The calcinated sample shows a maximum surface area of 177 m^2/g after calcination at 250 °C for 4 h. The surface area starts decreasing after calcination at a higher temperature. This shows the destruction of the pore structure may be due to heat agitation, leading to amorphous to crystalline phase transfer, which is evident from XRD. Further heating still reduces the surface area, and after heating at 500 °C we got a surface area 94 m^2/g. These results show that the mesostructure is stable even after removal of the surfactant, but it does not withstand the heat perturbation. A N_2 adsorption−desorption isotherm is given in Figure 5 at 77 K for the sample extracted for 12 h at elevated temperature (revealing the best surface area). The curve depicts a typical H2-type of hysteresis (according to IUPAC classification).[36] It may arise from the same type of open capillary branches that are responsible for H1-type of hysteresis, characteristics for the

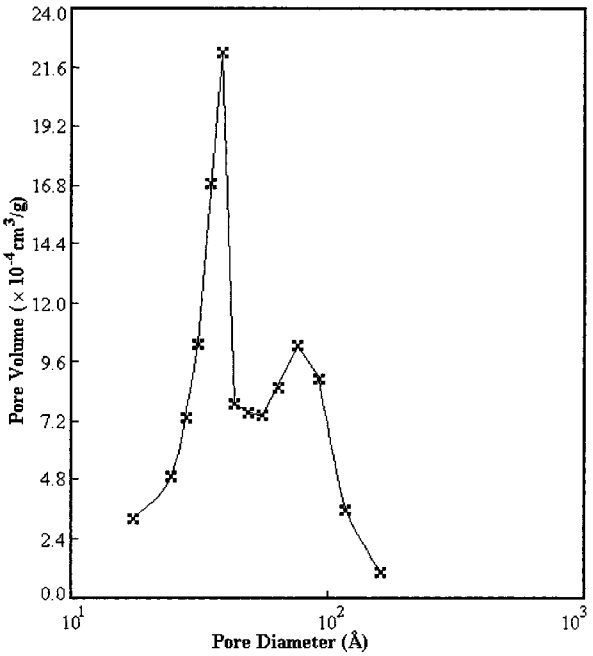

Figure 6. Pore size distribution for Fe_2O_3 mesostructure after extraction with ethanol for 12 h at elevated temperature.

examples of MCM-41.[37] However, the presence of H2-type hysteresis indicates that the effective radii of the mesoporous bodies are inhomogeneously distributed and the effective radii of the narrow entrance are of equal size. The H2-type of the hysteresis loop is typical for wormhole-structured materials. This further confirms the observation in the TEM studies. Figure 6 presents the pore size distribution for the same sample, obtained according to the Barrett−Joyner−Halenda (BJH) method using the Halsey equation for multilayer thickness.[36] This plot shows that the dominant peak is in the mesoporous range, with a narrow peak around 39 Å. Apart from this peak, we also observed a small peak at 75 Å. We concluded from this observation that though the samples are not so homogeneous, two dominant pore sizes are present in our sample. This result also supports our assumption of lack of long-range ordering, which we discussed as being the root cause of the absence of any peak in low angle XRD.

B. Magnetic Properties. Figure 7 shows the ^{57}Fe Mössbauer spectra (MS) of mesoporous iron oxides, which were calcinated at 250 °C and 500 °C. For the as-prepared sample (not shown), the spectrum exhibits only a broad doublet, which is attributed to Fe^{3+} in the high spin state, and indicates clearly that no long-range magnetic ordering is present. It is identical (within the range of uncertainty) to other Fe_2O_3 in the amorphous form published in the past.[38]

As stated above, after sonication the surfactant was removed by calcination at various temperatures. The MS obtained for the various calcinated samples are more complicated. Generally speaking, the spectra are composed of a broad sextet and a doublet. The relative intensity of the doublet decreases with temperature, and its hyperfine parameters are IS = 0.31 mm/s and QS = 1/2eq Q = 0.45 mm/s with the same line width (W) as for the sextet. The relative intensity of the doublet is ∼21 and 10%, for calcinations at 250 °C and 500 °C, respectively. The main effect seen in Figure 7 is the broad magnetic sextet obtained. This sextet is attributed to crystalline Fe_2O_3 (γ-Fe_2O_3) and the best fit is obtained when a distribution in the hyperfine magnetic field (H_{eff}) is assumed. The hyperfine parameters obtained are the following: (i) line width (W) = 0.55 mm/s,

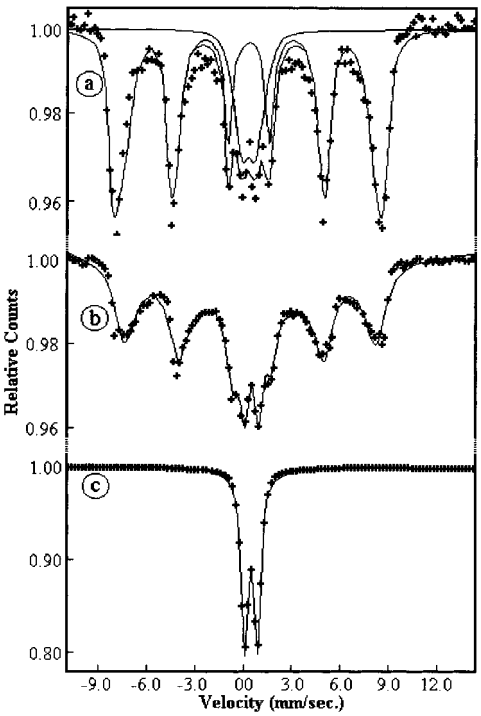

Figure 7. Mössbauer spectra of mesoporous iron oxides calcinated at (a) 250 °C, (b) 500 °C, and (c) for the solvent-extracted sample at room temperature.

(ii) IS = 0.30 mm/s, (iii) quadrupole splittings (QS) = 0, and (iv) an upper value for the magnetic field (H_{eff}) = 525(5) kOe. Similar hyperfine parameters have been obtained for the magnetic sub-spectrum of the 500 °C calcinated sample (Figure 7b). The distribution in the hyperfine values is a result of a non- uniform particle size obtained in the calcination process.

On the other hand, when the surfactant was removed by solvent extraction at ambient temperature, the MS obtained shows only one doublet (Figure 7c), which means that the material remains in its nonmagnetic form. The fit to the spectrum yields the hyperfine parameters: $W = 0.54$, IS = 0.51, and QS = 0.8 mm/s. These values are quite similar to the as-prepared sample discussed above.

The magnetizations vs field plots are given in Figure 8. The magnetization curve of the as-prepared and solvent-extracted sample (given in inset) shows a paramagnetic behavior. But the Figure 8a and 8b curves, which are for samples calcinated at 350 °C and 500 °C, respectively, show typical superparamagnetic behavior, without any hysteresis. The coercivity field and the remnant magnetization are found to be 2.5 G and 1.8 emu/g, respectively. At the same time, the curves do not show any saturation up to a 2.0 T field. This shows the conversion of nonmagnetic α-Fe_2O_3 (weak ferromagnetic at room temperature) into magnetic γ-Fe_2O_3 (ferrimagnetic at room temperature). Another conclusion that can be drawn from these observations is that the particle size is small enough to show the superparamagnetic behavior, as we concluded by MS and TEM studies. A possible explanation of the superparamagnetic behavior observed in the ferromagnetic material can be explained as follows: The local magnetic moments of the ferromagnetic materials are arranged in domains with a certain characteristic size. This yields a reduction in the magnetic energy of the demagnetizing field surrounding the sample. The total energy of the domain boundary is proportional to the square of the effective radius of a sample, whereas the magnetic energy of the demagnetization field shows the cubic proportionality. At a given particle, size the particles become single-domain (all spin oriented in a certain direction). In this case the material becomes superparamagnetic and does not exhibit saturation.

C. Catalytic Properties. We have examined the catalytic activity of mesoporous iron oxide in the oxidation of cyclohexane. We have previously reported on using amorphous nanosized iron,[39] cobalt,[39] iron oxide,[40] $Fe_{20}Ni_{80}$,[39] and Fe_2O_3 deposited in mesoporous titania,[33] as catalysts for the oxidation of cyclohexane. The details of the reaction are described in our earlier reports and are not repeated herein. In the currect investigation, under identical conditions, the mesoporous Fe_2O_3 catalyst shows the highest catalytic activity in comparison with all the nanostructured catalysts.[33,39−41] The reaction with mesoporous iron oxide obviously takes place by the same mechanism as that discussed for the nanostructured iron oxide catalyst.[40] The data for the oxidation of cyclohexane using different iron oxide catalysts are given in Table 2. Table 2 shows that the highest conversion of cyclohexane to products is obtained when the mesoporous iron oxide is used as the catalyst. It also demonstrates that the catalytic properties depend on a combination of factors such as particle size and surface area as well as the catalyst's structure. As it was shown previously, the calcinated (or crystalline) oxide is not active in the oxidation reaction. This is true for the calcinated mesoporous Fe_2O_3 as well. The conversion of cyclohexane on the new mesoporous catalysts is even higher than on iron oxide supported on mesoporous titania.[33] It is also worth noting that a better

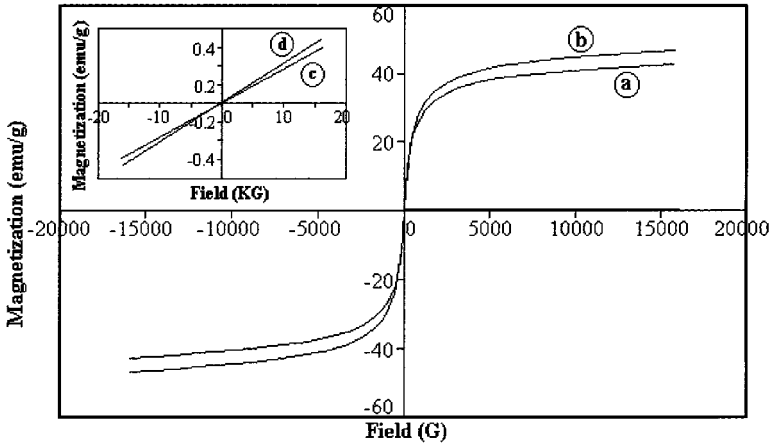

Figure 8. Room-temperature magnetization curve for (a) after calcination at 350 °C; (b) after calcination at 500 °C; (c) after extraction with ethanol for 12 h at room temperature; (d) as-prepared material.

TABLE 2: Oxidation of Cyclohexane Using Highly Dispersed Iron and Iron Oxide Catalysts (1 atm O_2, 70 °C)

catalyst[a]	particle size (nm)	surface area (m^2/g)	conversion (%)	Ol:one
Fe powder[c]	8−10		traces	
Fe_2O_3[c]	8−10	105	16.5	1.5:1
Fe_2O_3[d]	4−6	134	18.0	1.5:1
Fe_2O_3[d] (calcinated)	10−15	87	no traces	
Fe_2O_3 in msp TiO_2	100−200	570	25.8	1.5:1
Fe_2O_3 (msp)	100−200 (P.S. 3−5 nm)	274	35.6	5:1

[a] msp represents mesoporous. [b] Catalysts were prepared from solutions of iron pentacarbonyl in decaline. [c] 1 M. [d] 0.5 M.

selectivity is obtained with the new catalyst, as reflected in the Ol:One ratio.

IV. Conclusions

The sonochemical method for the preparation of Fe_2O_3 has been reported. The iron oxide was formed as amorphous α-Fe_2O_3, which was converted into γ-Fe_2O_3 after heating, with good magnetic properties. The surface area of the material has been found as high as 274 m^2/g after extraction of surfactant with ethanol. The extracted iron oxide has shown excellent catalytic properties in reaction of oxidation of cyclohexane.

Acknowledgment. D.N.S. thanks the Council of Higher Education of Israel, Jerusalem, for providing financial support in the form of a Postdoctoral Fellowship. Prof. A. Gedanken thanks the German Ministry of Science (BMBF) for support through the Deutsch-Isealische Projekt partnerschaft (DIF). We also thank Ms. Louise Braverman for editorial assistance.

References and Notes

(1) Castano, J. G.; Arroyave, C. *Rev. Metal.* **1998**, *34*, 274.
(2) Frank, S.; Lauterbur, P. C. *Nature* **1993**, *363*, 334.
(3) Tifenauer, L. X.; Tschirky, A.; Kuhne, G.; Andres, R. Y. *Magn. Reson. Imaging* **1996**, 14, 391.
(4) Yamaguchi, K.; Matsumoto, K.; Fujii, T. *J. Appl. Phys.* **1990**, *67*, 4493.
(5) Maruyama, T.; Kanagawa, T. *J. Electrochem. Soc.* **1996**, *143*, *1675*.
(6) Prinz, G. A. *Science* **1998**, *282*, 1660.
(7) Moriarty, P. *Rep. Prog. Phys.* **2001**, *64*, 297.
(8) Kreage, C. T.; Leonowicz, M. E.; Roth, W. J.; Vartuli, J. C.; Beck, J. S. *Nature* **1992**, *359*, 710.
(9) Ying, J. Y.; Mehnert, C. P.; Wong, M. S. *Angew. Chem. Int. Ed.* **1999**, *38*, 56.
(10) Cosnier, S.; Senillou, A.; Gratzel, M.; Comte, P.; Vlachopoulos, N.; Renault, N. J.; Mortelet, C. *J. Electroanal. Chem.* **1999**, *469*, 176.
(11) Cosnier, S.; Gondran, C.; Senillou, A.; Gratzel, M.; Vlachopoulos, N. *Electroanalysis* **1997**, *9*, 1387.
(12) Innocenzi, P.; Martucci, A.; Guglielmi, M.; Bearzotti, A.; Traversa, E. *Sensor Actuat B−Chem.* **2001**, *76*, 299.
(13) Keefe, M. H.; Slone, R. V.; Hupp, J. T.; Czaplewski, K. F.; Snurr, R. Q.; Stem, C. L. *Langmuir* **2000**, *16*, 3964.
(14) Shiraishi, S.; Kurihara, H.; Oya, A. *Electrochemistry* **2001**, *69*, 440.
(15) Yoon, S.; Lee, J. W.; Hyeon, T.; Oh, S. M. *J. Electrochem. Soc.* **2000**, *147*, 2507.
(16) Choi, H. J.; Cho, M. S.; Kang, K. K.; Ahn, W. S. *Microporous Mesoporous Mater*. **2000**, *39*, 19.
(17) Gratzel, M. *Curr. Opin. Colloid Sci*. **1999**, *4*, 314.
(18) Bach, U.; Lupo, D.; Comte, P.; Moser, J. E.; Weissortel, F.; Salbeck, J.; Spreitzer, H.; Gratzel, M. *Nature* **1998**, *395*, 583.
(19) Papageorgiou, N.; Barbe, C.; Gratzel, M. *J. Phys. Chem. B* **1998**, *102*, 4156.
(20) Wang, Y. Q.; Chen, S. G.; Tang, X. H.; Palchik, O.; Zaban, A.; Koltypin, Y.; Gedanken, A. *J. Mater. Chem.* **2001**, *11*, 521.
(21) Gratzel, M. *Pure Appl. Chem.* **2001**, *73*, 459.
(22) Morris, C. A.; Anderson, M. L.; Stroud, R. M.; Merzbacher, C. I.; Rolison, D. R. *Science* **1999**, *284*, 622.
(23) Jiang, P.; Hwang, K. S.; Mittleman, D. M.; Bertane, J. F.; Colvin, V. L. *J. Am. Chem. Soc.* **1999**, *121*, 11630.
(24) MacLachlan, M. J.; Ginzburg, M.; Coombs, N.; Raju, N. P.; Greedan, J. E.; Ozin, G. A.; Manners, I. *J. Am. Chem. Soc*. **2000**, *122*, 3878.
(25) Vettraino, M.; He, X.; Trudeau, M.; Antonelli, D. M. *J. Mater. Chem.* **2001**, *11*, 1755.
(26) Tolbert, S. H.; Sieger, P.; Stucky, G. D.; Aubin, S. M. J.; Wu, C. C.; Hendrickson, D. N. *J. Am. Chem. Soc.* **1997**, *119*, 8652.
(27) Murray, S.; Trudeau, M.; Antonelli, D. M. *Inorg. Chem.* **2000**, *39*, 5901.
(28) Sun, Q. H.; Lam, J. W. Y.; Xu, K. T.; Xu, H. Y.; Cha, J. A. K.; Wong, P. C. L.; Wen, G. H.; Zhang, X. X.; Jing, X. B.; Wang, F. S.; Tang, B. Z. *Chem. Mater.* **2000**, *12*, 2617.
(29) Li, S.; Meitzner, G. D.; Iglesia, E. *J. Phys. Chem. B* **2001**, *105*, 5743.
(30) Pal, B.; Sharon, M. *Thin Solid Films* **2000**, *379*, 83.
(31) Yin, J. Y.; Mehnert, C. P.; Wong, M. S. *Angew. Chem. Int. Ed.* **1999**, *38*, 56.
(32) Carma, A.; *Chem. Rev.* **1997**, *97*, 2373.
(33) Perkas, N.; Wang, Y. Q.; Koltypin, Y.; Gedanken, A.; Chandrasekaran, S. *Chem. Commun*. **2001**, *11*, 988.
(34) Zysler, R. D.; Mansilla-Vasquez, M.; Arciprete, C.; Dimitrijewits, M.; Rodriguez-Sierra, D.; Saragovi, C. *J. Magn. Magn. Mater*. **2001**, *224*, 39.
(35) Cao, X.; Prozorov, R.; Koltypin, Y.; Kataby, G.; Felner, I.; Gedanken, A. *J. Mater. Res.* **1997**, *12*, 402.
(36) Sing, K. S. W.; Everett, D. H.; Haul, R. A. W.; Moscou, L.; Pietotti, R. A.; Rouquerol, J.; Siemienieska, T. *Pure Appl. Chem.* **1985**, *57*, 603.
(37) Blin, J. L.; Leonard, A.; Su, B. L. *J. Phys. Chem. B* **2001**, *105*, 6070.
(38) Zhong, Z. Y.; Prozorov, T.; Felner, I.; Gedanken. A. *J. Phys. Chem. B* **1999**, *103*, 947.
(39) Kesavan, V.; Sivanand, P. S.; Chandtasekaran, S.; Koltypin, Y.; Gedanken, A. *Angew. Chem. Int. Ed.* **1999**, *38*, 3521.
(40) Perkas, N.; Koltypin, Y.; Palchik, O.; Gedanken, A.; Chandrasekaran, S. *Appl. Catal. A: General* **2001**, *209*, 125.
(41) Murahashi, S. T.; Oda, Y.; Naota, T. *J. Am. Chem. Soc*. **1992**, *114*, 7913.